

Recombination properties of oxygen-precipitated silicon^{a)}

J. M. Hwang and D. K. Schroder

Center for Solid-State Electronics Research, Arizona State University, Tempe, Arizona 85287

(Received 29 July 1985; accepted for publication 9 December 1985)

It is well known that recombination lifetimes are significantly degraded in oxygen-precipitated silicon. The possible sources for lifetime degradation are expected to be oxygen precipitates (OP's), dislocation loops, stacking faults, and point defects associated with self-interstitials generated during the oxygen precipitation process. From the results of an extensive experimental study using IR absorption, TEM, DLTS, and SPV (surface photovoltage), we have found that OP's are mainly responsible for the observed lifetime degradation and that recombination at OP's takes place through Si/OP interface states. In addition we have observed that the lifetime degradation is more severe in *p*-Si than in *n*-Si even for identical densities and sizes of OP's. A model for recombination at OP's is presented in terms of the surface recombination velocity at the Si/OP interface and their average density and size. To explain the lifetime difference between *n*-Si and *p*-Si we propose a band bending around OP's caused by positive fixed charges in the OP's.

<https://doi.org/10.1063/1.336993>

I. INTRODUCTION

Dislocation-free, Czochralski-grown silicon contains oxygen as a predominant impurity in concentrations of typically 5×10^{17} – $2 \times 10^{18} \text{ cm}^{-3}$,¹ which is close to the solid solubility at the Si melt temperature of 1414 °C. Atomic oxygen is located on interstitial sites between two neighboring Si atoms in the [111] directions,² and it is not electrically active. At elevated temperatures, the supersaturated interstitial oxygen precipitates and forms oxygen precipitates (OP's) with SiO_x chemical composition ($1 < x < 2$) inside the Si crystal.

Oxygen precipitates have been extensively investigated in the past, because of their beneficial and detrimental effects on device performance. They are reasonably well understood in terms of nucleation,^{3–5} growth,^{6–8} morphology,^{9–14} and chemical composition.^{15–17} Secondary defects caused by OP's, such as dislocation loops and extrinsic stacking faults have also been extensively studied.^{9–11,18–20}

One of the advantages of oxygen in silicon is the intrinsic gettering³⁷ which is usually achieved by a three-step "high-low-high" thermal cycle.^{21,38} During the first high-temperature anneal (about 1100 °C), the oxygen near the surface diffuses out, forming a denuded zone of typically 10–20 μm. The subsequent low- (650–750 °C) and high- (about 1000 °C) temperature anneals are for the nucleation and growth of OP's, respectively, in the bulk region where a high supersaturation of oxygen is maintained. The OP's and secondary defects play a role for gettering metallic impurities from the device-active layer near the wafer surface.

It is frequently claimed that the precipitated bulk region is unimportant for device operation which takes place in the top few microns determined essentially by the width of the space-charge region. This is generally correct for room-temperature operation. However, it is not true for operation at temperatures above about 70 °C in which the leakage current contribution from the bulk region becomes important.^{23,26,27,39} This bulk leakage current is the diffusion cur-

rent associated with the recombination lifetime (τ_r) while the generation current in the space-charge region is characterized by the generation lifetime (τ_g). Therefore, there is a need for understanding the recombination properties of the precipitated bulk region.

The formation of OP's in the wafer bulk degrades both the recombination as well as the generation lifetime. This has been reported using the pulsed MOS capacitor method,^{22,23} the diode recovery method,²⁴ the photoconductive decay method,²⁵ the surface photovoltage method,²⁶ and the measurement of the diode leakage current.²⁷ But it has not yet been definitely established what causes the lifetime degradation. Some results suggest that a discrete energy level is introduced into the band gap,²⁸ that appears to correlate with a level formed by dislocations. Other results²⁹ point to a continuous distribution of energy levels throughout the band gap, caused most likely by interface states at the Si/OP interface. However, there are as yet no clear, unambiguous answers to the questions:

(1) What is the dominant source for the lifetime degradation: the OP's themselves, secondary defects like dislocation loops or stacking faults, or point defects associated with Si self-interstitials?^{18,19,30}

(2) How is the carrier lifetime related to the density and size of OP's and the properties of the Si/OP interface?

(3) Are there any distinct differences between the conventional Si-SiO₂ interface with its reasonably well understood interface states and the Si/OP interface?

We have used deep level transient spectroscopy (DLTS), surface photovoltage (SPV), IR absorption, and transmission electron microscopy (TEM) to unravel these questions. IR absorption is used to monitor the oxygen concentration, DLTS to identify generation-recombination centers, TEM to characterize structural defects such as OP's, dislocation loops and stacking faults, and SPV to measure the minority carrier diffusion length.

II. EXPERIMENTAL DETAILS

The wafers used in this work are Cz-grown, boron-doped, and phosphorus-doped Si of 3 in. diam. The *p*-type

^{a)} This work was partially supported by NSF Grant ECS-82-12336.

wafers were of $10\ \Omega\text{ cm}$ resistivity with initial interstitial oxygen concentration of $9 \times 10^{17}\text{ cm}^{-3}$ and initial substitutional carbon concentration of $7.5 \times 10^{16}\text{ cm}^{-3}$. For the n -type wafers these values were $8\ \Omega\text{ cm}$, $8 \times 10^{17}\text{ cm}^{-3}$, and $5.2 \times 10^{16}\text{ cm}^{-3}$. The oxygen and carbon concentrations were determined from FTIR measurements using a Nicolet 10-MX Instrument using the ASTM F121-80 and ASTM F123-81 conversion factors, respectively.

To induce a variety of OP's into the wafers, various annealing cycles were carried out, as summarized in Table I. After each anneal, the oxygen and carbon concentrations were measured at room temperature. The wafers were divided into 5 groups: A–E. Since we were interested in studying the bulk precipitation, we did not subject the wafers to the first “high” oxygen out-diffusion anneal.

Wafer A was annealed at a low temperature in a variety of gas ambients. The others were subjected to a “low-high” sequence. In each case, the “low” anneal was at a given temperature and the “high” anneal was done either at various temperatures in a given gas ambient, or at a given temperature in a variety of gas ambients. For a given sequence, we performed the “low” anneal and then broke the wafer into 4 quarters and subjected the resulting sections to the “high” anneal cycle. This was done to assure that the samples in a given set were as uniform as can be expected from one wafer. This is preferred over the use of different wafers, coming from different parts of the ingot, that show larger variations.

After annealing, about $25\ \mu\text{m}$ was etched from the wafer surfaces to remove any denuded zones that might have formed. Then a small piece was cut from each sample for Schottky diode fabrication for DLTS measurements. For p -type samples, Al was sputtered through a metal mask while for the n -type samples gold was evaporated through the mask. The device area was $2.3 \times 10^{-3}\text{ cm}^2$. Back contacts were made by sputtering Al on the wafer back for both types. In order not to subject the wafers used for DLTS to additional anneals, the wafers were not subjected to an alloy heat cycle after metal deposition. There is therefore the possibility for the back contact to act as a rectifying contact. This is not of any consequence, since first of all it is of very large area

and secondly, during DLTS measurements it is forward biased with an attendant very high capacitance which is in series with the much smaller device capacitance. Devices for the DLTS study were selected from similar positions on each sample.

The DLTS system uses a lock-in amplifier for signal integration, with a gate-off function to eliminate the large but uninformative portion of the capacitance signal corresponding to the capture period.^{32,33} The SPV was measured with a computer-controlled system.³⁴ TEM measurements were made on selected samples to characterize structural defects that might have been generated during the anneals.

III. EXPERIMENTAL RESULTS

A. IR absorption

The results of the IR measurements are shown in Table II with the solid solubility values calculated from Craven's data³⁵:

$$[O_i]_s = 1.53 \times 10^{21} \exp(-1.03/kT). \quad (1)$$

In the sample group A, subjected to a single-step $800^\circ\text{C}/96\text{ h}$ anneal, the oxygen concentration decreases almost to the solubility value and the substitutional carbon reduces below the detection limit of 10^{16} cm^{-3} (0.2 ppm). The gas ambient during this anneal had very little effect on oxygen precipitation.

In sample group B, the first anneal at $800^\circ\text{C}/48\text{ h}$ causes a significant reduction of $[O_i]$ to 2 ppm. Subsequent anneals at 950, 1050, and 1150°C increased that value, with the 950°C showing the smallest increase. This is due to the redissolution of precipitated oxygen since the concentration of interstitial oxygen remaining after the prolonged first anneal is smaller than or almost equal to the solid solubility values at each second-anneal temperature. Therefore, most of the OP's formed during the first anneal are believed to have shrunk during the second anneal. The redissolution rate increases with anneal temperature because the oxygen diffusion is the rate-limiting process.³¹

In sample groups C and E, even after the first $750^\circ\text{C}/10\text{ h}$ anneal, a high degree of supersaturation is still maintained

TABLE I. Sample designations and anneals.

Sample		First anneal	Second anneal
A (p type)	S7-1	$800^\circ\text{C}/96\text{ h N}_2$...
	S7-2	$800^\circ\text{C}/96\text{ h O}_2$...
	S7-3	$800^\circ\text{C}/96\text{ h O}_2 + 5\% \text{ HCl}$...
B (p type)	S6-1	$800^\circ\text{C}/48\text{ h O}_2$	$950^\circ\text{C}/4\text{ h O}_2$
	S6-2	$800^\circ\text{C}/48\text{ h O}_2$	$1050^\circ\text{C}/4\text{ h O}_2$
	S6-3	$800^\circ\text{C}/48\text{ h O}_2$	$1150^\circ\text{C}/4\text{ h O}_2$
C (p type)	S27-1	$750^\circ\text{C}/10\text{ h O}_2$	$1050^\circ\text{C}/16\text{ h N}_2$
	S27-2	$750^\circ\text{C}/10\text{ h O}_2$	$1050^\circ\text{C}/16\text{ h O}_2$
	S27-3	$750^\circ\text{C}/10\text{ h O}_2$	$1050^\circ\text{C}/16\text{ h O}_2 + 5\% \text{ HCl}$
D (n type)	N1-1	$750^\circ\text{C}/10\text{ h O}_2$	$850^\circ\text{C}/16\text{ h O}_2$
	N1-2	$750^\circ\text{C}/10\text{ h O}_2$	$1050^\circ\text{C}/16\text{ h O}_2$
	N1-3	$750^\circ\text{C}/10\text{ h O}_2$	$1150^\circ\text{C}/16\text{ h O}_2$
E (n type)	N2-1	$750^\circ\text{C}/10\text{ h O}_2$	$1050^\circ\text{C}/16\text{ h N}_2$
	N2-2	$750^\circ\text{C}/10\text{ h O}_2$	$1050^\circ\text{C}/16\text{ h O}_2$
	N2-3	$750^\circ\text{C}/10\text{ h O}_2$	$1050^\circ\text{C}/16\text{ h O}_2 + 5\% \text{ HCl}$

TABLE II. $[O_i]$ and $[C_s]$ measured by FTIR.

Sample	$[O_i]$ (ppm)	$[C_s]$ (ppm)	$[O_i]_s^*$ (ppm)	T (°C)
A	as-grown	17.7	2.2	
	S7-1	1.0	<0.2	800
	S7-2	0.9	<0.2	800
	S7-3	1.0	<0.2	800
B	as-grown	17.7	2.2	
	first anneal	2.0	<0.2	800
	S6-1	2.2	<0.2	950
	S6-2	2.6	<0.2	1050
	S6-3	5.1	<0.2	1150
C	as-grown	17.2	2.5	
	first anneal	15.1	1.6	
	S27-1	7.0	0.9	1050
	S27-2	6.7	0.9	1050
	S27-3	6.4	0.6	1050
D	as-grown	15.1	0.8	
	N1-1	3.6	<0.2	950
	N1-2	8.0	<0.2	1050
	N1-3	9.7	0.3	1150
E	as-grown	14.6	1.2	
	N2-1	6.8	1.0	1050
	N2-2	7.2	1.1	1050
	N2-3	7.2	0.8	1050

*Solid solubilities calculated from Eq. (1) for corresponding anneal temperatures.

and subsequent high-temperature anneals at 1050 °C give rise to further oxygen precipitation.

Sample group D demonstrates the effect of the second-anneal temperature on precipitation. The precipitation rate decreases with increasing second-anneal temperature, although oxygen diffuses faster at higher temperatures. This may be interpreted in the following way: The OP's formed during the first anneal are presumed to have a size distribution. In the second anneal, the OP's larger than a critical size grow, while those smaller than the critical size shrink and eventually disappear after a certain period of time.^{5,7} The thermodynamic quantity, the critical size, increases with annealing temperature for a given concentration of supersaturated oxygen.^{3,4} Consequently, a lower temperature anneal will allow a higher density of OP's to grow continuously, while in a higher temperature anneal a limited number of OP's will grow and the rest will dissolve, resulting in less precipitation.

B. TEM results

Groups A, C, and E were examined by TEM. As expected, the group A samples show a high density of small-sized OP's. Densities are found to be of the order of 10^{13} cm^{-3} . It is difficult to estimate the average OP sizes in these samples because of their small dimension ($< 100 \text{ Å}$ in diameter).

In the samples of group C (p type) and E (n type) the average OP densities are found to be in the range of 10^{11} – 10^{12} cm^{-3} with average sizes of roughly 100 to 200 Å. Most of the OP's have the well-known octahedral shape bounded by eight $\{111\}$ planes,¹³ except for very few large-sized plate-like OP's with $\{100\}$ habit planes that are often accompanied by prismatic dislocation loops.⁹ A relatively high car-

bon content in our samples appears to be responsible for the formation of octahedral OP's.^{12,14} We approximate the octahedral shape by a spherical one in further discussions.

Since in general, the average OP densities can be more easily estimated than the average sizes, we first determine the OP densities from TEM micrographs and then calculate the corresponding average OP sizes using the following relationship derived on the basis of conservation of oxygen atoms³⁶:

$$\frac{4}{3}\pi r_0^3 C_p N_{op} = [O_i]_i - [O_i]_f, \quad (2)$$

where r_0 denotes the average radius of OP's, C_p the atomic density of oxygen in an OP, N_{op} the average OP density, $[O_i]_i$ and $[O_i]_f$ the initial and final concentration of interstitial oxygen, respectively. In actual calculations $C_p = 4.5 \times 10^{22} \text{ cm}^{-3}$ was used with the assumption that OP's have the SiO_2 chemical composition. The average OP densities and sizes obtained in such a way are summarized in Table III. For the sample group C and E the calculated OP sizes are in reasonable agreement with the estimated ones on the TEM micrographs.

In all the samples examined by TEM, secondary defects like dislocation loops or stacking faults were rarely observed. But stacking faults were observed on Secco-etched cross sections for the samples annealed at high temperatures of 1050 and 1150 °C with a density of about 10^8 cm^{-3} . Their density is much smaller compared with that of OP's so that their influence on DLTS spectra or recombination lifetimes may be neglected.

C. DLTS results

The three samples of group A show almost the same DLTS spectra regardless of ambient as shown in Fig. 1. Considering that the half-width of a normal DLTS peak for a discrete energy level is given by one tenth of the peak temperature T_p ($\Delta T \approx 0.1 T_p$), this broad peak indicates a continuous distribution of energy states in the band gap whose amplitude gradually increases toward the valence-band edge, reaches its maximum at about $E_v + 0.08 \text{ eV}$, and then decreases toward the band edge.

DLTS spectra for the samples of group B are shown in Fig. 2, where the effects of the second-anneal temperature become clear. The spectrum of the sample S6-1 annealed at 950 °C appears to be almost the same as that of the group A samples annealed at 800 °C. As the second-anneal temperatures increases, the amplitude of the broad peak around 60 K appears to be reduced. In sample S6-3 annealed at 1150 °C

TABLE III. Average densities and sizes of OP's.

Sample	Average OP density (cm^{-3})	Average radius (Å)
A	S7-1	3.0×10^{13}
	S7-2	2.6×10^{13}
C	S27-1	2.6×10^{12}
	S27-2	1.7×10^{12}
E	N2-1	1.1×10^{12}
	N2-2	2.3×10^{12}

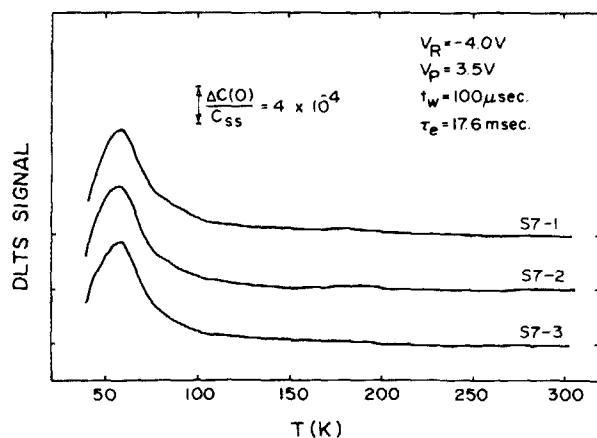


FIG. 1. DLTS spectra for group A samples (*p* type): one-step anneal; 800 °C/96 h for three different ambients, N₂ (S7-1), O₂ (S7-2), and O₂ + HCl (S7-3). Captional notations mean C_{ss} = steady-state capacitance, $\Delta C(0)$ = capacitance change due to deep traps at $t = 0$ when the pulse is terminated, V_R = reverse bias, V_P = pulse amplitude, t_w = pulse width, and τ_e = peak emission time constant.

this broad peak completely disappears and instead another broader spectrum shape corresponding to an energy range over the lower half of the band gap appears with small amplitude. Figure 3 shows DLTS spectra for the group C samples. The broad distribution of energy states near midgap is similar to that of S6-3 in Fig. 2.

DLTS spectra for the *n*-type samples of group D are shown in Fig. 4. The sample N1-1 annealed at 850 °C shows a continuous distribution of energy states whose density increases monotonically toward the conduction-band edge. Similar DLTS spectra have recently been reported by Hoelzlein *et al.*²⁹ who investigated new thermal donors formed during prolonged anneals at 650 °C in *n*-type silicon. Unlike the *p*-type case shown in Fig. 1, a density peak near the conduction-band edge is not seen. The sharp decrease of the spectra at low temperatures below 40 K is more likely to be due to the freeze-out of free carriers. It is noted that as the second-anneal temperature increases, the DLTS signal re-

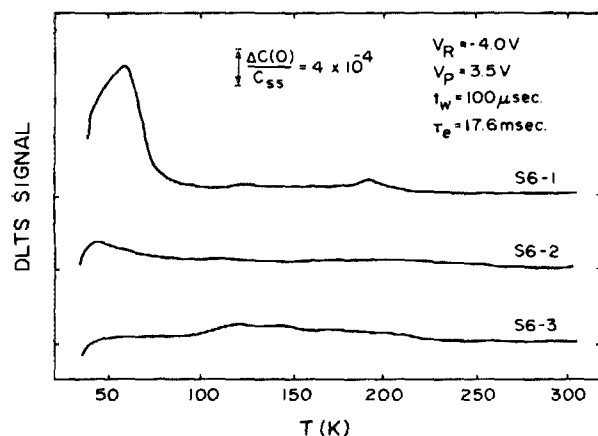


FIG. 2. DLTS spectra for group B samples (*p* type): two-step anneal; 800 °C/48 h O₂ + 950 °C (S6-1), 1050 °C (S6-2), and 1150 °C (S6-3)/4 h O₂.

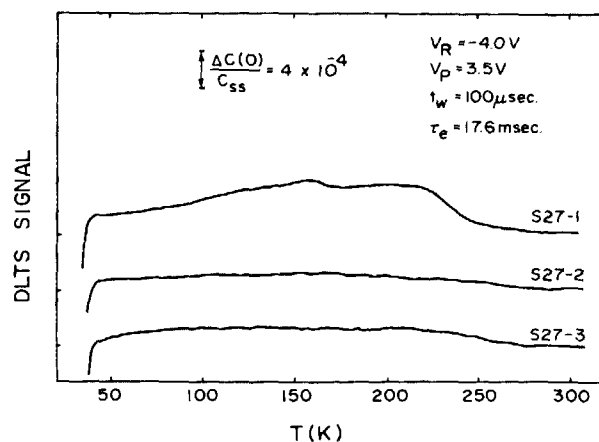


FIG. 3. DLTS spectra for group C samples (*p* type): two step anneal; 750 °C/10 h O₂ + 1050 °C/16 h for three different ambients, N₂ (S27-1), O₂ (S27-2), and O₂ + HCl (S27-3).

duces significantly, especially the portion of the states near the band edge. This implies a strong correlation between the DLTS output and the OP density, both of which decrease with the second-anneal temperature.

Figure 5 shows DLTS spectra of the group E samples for three different ambients. No distinguishable difference between three spectra is found within experimental error. Because of similar annealing conditions the spectra are identical to that of N1-2 in Fig. 4.

D. Diffusion length measurements

Diffusion lengths (L) measured by the SPV technique and the corresponding effective lifetimes (τ_{eff}) are shown in Table IV. Effective lifetimes were calculated from measured diffusion lengths using the equation $\tau_{eff} = L^2/D$ with $D_n = 30 \text{ cm}^2/\text{s}$ for the electron and $D_p = 10 \text{ cm}^2/\text{s}$ for the hole diffusion coefficient. As-grown samples were found to have diffusion lengths in the range of 150–200 μm in *p*-type and 220–230 μm in *n*-type samples. However, in the oxygen-precipitated samples the diffusion lengths decreased drasti-

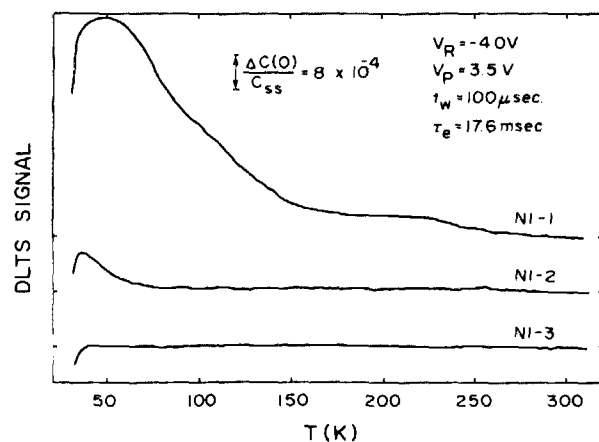


FIG. 4. DLTS spectra for group D samples (*n* type): two-step anneal; 750 °C/10 h O₂ + 850 °C (N1-1), 1050 °C (N1-2), and 1150 °C (N1-3)/16 h O₂.

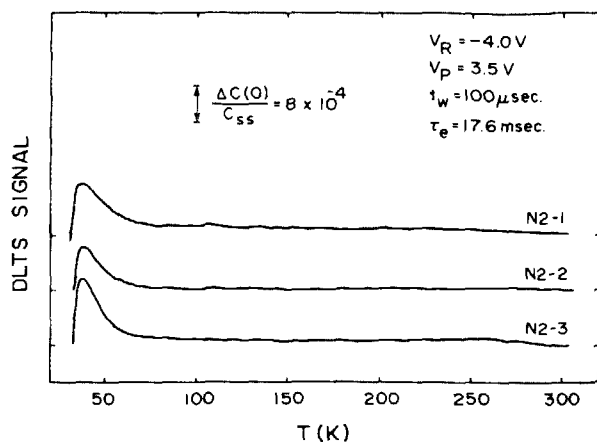


FIG. 5. DLTS spectra for group E samples (*n* type): two-step anneal; 750 °C/10 h O₂ + 1050 °C/16 h for three different ambients, N₂ (N2-1), O₂ (N2-2), and O₂ + HCl (N2-3).

cally. Moreover, the degradation of the diffusion lengths or lifetimes is, as a whole, much more severe in *p*-type than in *n*-type silicon. Diffusion lengths in *p* type are reduced by about two orders of magnitude compared to those in as-grown samples, but in *n* type they degrade only by an order of magnitude. This corresponds to effective recombination lifetimes of the order of nanoseconds in *p* type and microseconds in *n* type.

The lifetime differences are more clearly seen in Fig. 6 where the dependences of lifetime on second-anneal temperature are illustrated for group B (*p* type) and group D (*n* type). The lifetime data for the samples of group C and group E which received identical two-step heat treatments except for the gas ambient, fit reasonably well on the curves for *p*-Si and *n*-Si, respectively. The temperature dependence of the lifetime appears to be consistent with the corresponding DLTS results. In other words, as the second-anneal temperature increases, N_{op} decreases, leading to the DLTS signal decrease (see Figs. 2 and 4) and the lifetime increase.

TABLE IV. Minority-carrier diffusion lengths and recombination lifetimes measured by SPV.

Sample	L (μm)	τ_{eff}^* (μs)
A S7-1	1.4	0.7×10^{-3}
	1.6	0.8×10^{-3}
B S6-1	1.5	0.7×10^{-3}
	2.3	1.8×10^{-3}
	2.2	1.6×10^{-3}
C S27-1	2.4	1.9×10^{-3}
	2.3	1.8×10^{-3}
	2.6	2.2×10^{-3}
D N1-1	5.8	0.03
	30.1	0.9
	33.2	1.1
E N2-1	22.6	0.5
	28.1	0.8
	33.9	1.2

* $\tau_{eff} = L^2/D$ ($D_p = 10 \text{ cm}^2/\text{s}$, $D_n = 30 \text{ cm}^2/\text{s}$).

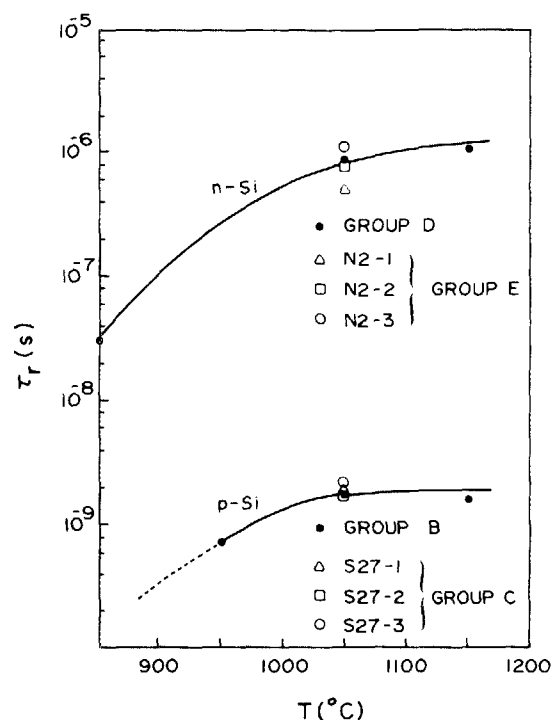


FIG. 6. Second-anneal temperature dependence of recombination lifetime for *p*-type samples (group B) and for *n* type samples (group D). Recombination lifetimes for group C (*p* type) and group E (*n* type) samples annealed at 1050 °C fit reasonably well on the curves.

From this increasing lifetime with annealing temperature it is obvious that the degradation of lifetime is not mainly caused by contamination of metallic impurities during the anneal process. Both the diffusion coefficient and solubility of metallic impurities increase with increasing temperature. Hence, we would expect more contamination and lower lifetimes for the higher anneal temperatures. The opposite is observed.

IV. DISCUSSION

The formation of OP's in the bulk accompanies a local volume expansion that results in a compressive stress toward the Si matrix at the Si/OP interface. Such a stress inside the crystal can be released by generating dislocation loops, absorbing vacancies, and/or emitting Si self-interstitials.^{10,40,41} Extrinsic stacking faults that are often observed in oxygen-precipitated silicon are strong evidence for the emission of self-interstitials because they are a condensed precipitate form of supersaturated self-interstitials.^{18,19,30}

Therefore, the possible sources for lifetime degradation in oxygen-precipitated silicon are expected to be structural defects such as dislocation loops, stacking faults, and OP's themselves, as well as point defects associated with silicon self-interstitials such as *di*-interstitials^{42,43} and complex forms with other intrinsic impurities like carbon, oxygen, or dopant atoms.

However, if we assume that the lifetime degradation is caused by point defects, its concentration leading to our measured lifetimes must be approximately $5 \times 10^{16} \text{ cm}^{-3}$ in *p*-type and 10^{14} cm^{-3} in *n*-type samples using a typical cap-

ture cross-section value of 10^{-15} cm^2 . If the wafers contained such high densities, we should have observed a huge amplitude of discrete DLTS peaks. In reality, we did not observe such a high density of point defects but instead we observed broad DLTS spectra corresponding to a continuum of energy states. The experimental results showed that both the broad DLTS signal and the recombination lifetime are strongly correlated to the OP density. Furthermore, TEM results showed that dislocation loops or stacking faults are rarely present in the samples under consideration. As a consequence it is concluded that the broad DLTS spectra are due to Si/OP interface states which are similar to conventional Si/SiO₂ interface states and are the major generation-recombination centers responsible for the observed lifetime degradation.

A. Silicon/oxygen precipitate interface states

The energy distribution of generation-recombination centers continuously distributed through the band gap, can be determined from the DLTS signal. The determination of the interface state density for the conventional Si/SiO₂ interface is well established.⁴⁴⁻⁴⁸ Hoelzlein *et al.*²⁹ applied the principle to Si/OP interface states. Here, we will show the results derived for the DLTS system used in this work.

Let D_{br} be the bulk state density with units $\text{cm}^{-3} \text{ eV}^{-1}$. Then, the equivalent bulk trap concentration N_{eq} that would give the same DLTS output at a specific temperature is given by

$$N_{eq} = 2.94 kTD_{br}(E). \quad (3)$$

This physically means that the interface states within the energy interval given by $\Delta E = 2.94 kT$ contribute effectively to the DLTS signal at temperature T . N_{eq} is measured in the same way as discrete energy levels. Once $D_{br}(E)$ is determined, the conventional interface state density $D_{it}(E)$ in units of $\text{cm}^{-2} \text{ eV}^{-1}$ is obtained as

$$D_{it}(E) = D_{br}(E)/(N_{op} \times A_{op}), \quad (4)$$

where N_{op} denotes the OP density and A_{op} its average surface area. For example, let us consider the *p*-type sample (S7-1) and the *n*-type sample (N1-1) which show a relatively large amplitude of DLTS signals. From the DLTS signal for S7-1 (Fig. 1) the equivalent bulk concentration at $T = 60 \text{ K}$ is determined as $N_{eq} = 6.5 \times 10^{12} \text{ cm}^{-3}$ so that $D_{br} = 4.3 \times 10^{14} \text{ cm}^{-3} \text{ eV}^{-1}$ by Eq. (3) and $D_{it} = 4.0 \times 10^{12} \text{ cm}^{-2} \text{ eV}^{-1}$ by Eq. (4) for $N_{op} = 3.0 \times 10^{13} \text{ cm}^{-3}$ and OP radius $r_0 = 54 \text{ \AA}$. From the DLTS spectrum for N1-1 (Fig. 5) $N_{eq} = 5.8 \times 10^{12} \text{ cm}^{-3}$ at $T = 50 \text{ K}$ so that $D_{br} = 4.6 \times 10^{14} \text{ cm}^{-3} \text{ eV}^{-1}$ and $D_{it} = 2.0 \times 10^{13} \text{ cm}^{-2} \text{ eV}^{-1}$ with the assumption of $N_{op} = 3.0 \times 10^{13} \text{ cm}^{-3}$ and $r_0 = 50 \text{ \AA}$.

Next, we need to determine the energy levels of the interface states for a specific DLTS temperature at which D_{it} is obtained. If a DLTS spectrum varies distinctively with temperature, the energies can be determined in the same way as those of discrete bulk defects. In other words, they can be determined from the Arrhenius plot by varying the rate window. This technique is, however, not suitable for slowly varying or constant DLTS spectra with temperature, which

are common for the Si/SiO₂ interface states with a continuum of energy states. So, in this work the energy levels are calculated using the balance equation for the emission rate with the assumption of a constant capture cross section through the energy range of interest. The emission rates for electrons and holes are given by

$$e_n = v_n \sigma_n N_c \exp[-(E_c - E_T)/kT] \quad (5)$$

and

$$e_p = v_p \sigma_p N_v \exp[-(E_T - E_v)/kT], \quad (6)$$

respectively, where v_n is the electron thermal velocity, σ_n the capture cross section, N_c the effective density of states in the conduction band, E_c the minimum energy of the conduction band, and E_T the trap energy level. Analogous definitions apply for holes.

The emission rate e_0 , which gives rise to a DLTS peak, is related to the rate window by $e_0^{-1} = 0.44 t_p$ for our system, where t_p is the pulse period of the lock-in system. Therefore, if a proper value of capture cross section is chosen one can calculate the energy level for D_{it} measured at a temperature, by using Eq. (5) or Eq. (6).

Figures 7 and 8 show the Si/OP interface state density distributions obtained in such a way. Figure 7 is for the *p*-type samples, S7-1 (800 °C/96 h N₂) and S27-1 (750 °C/10 h O₂ + 1050 °C/16 h N₂), using $\sigma_p = 10^{-16} \text{ cm}^2$. Figure 8 is for the *n*-type samples, N1-1 (750 °C/10 h O₂ + 850 °C/16 h O₂) and N2-1 (750 °C/10 h O₂ + 1050 °C/16 h N₂), using $\sigma_n = 10^{-15} \text{ cm}^2$. Considering simultaneously both of the

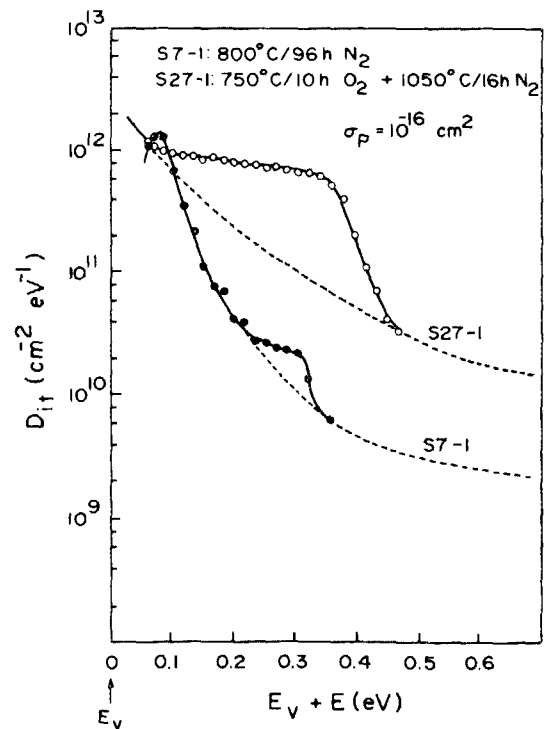


FIG. 7. Density distributions of Si/OP interface states in the lower half of band gap obtained from the DLTS spectra shown in Figs. 1 and 3 for two typical *p*-type samples, S7-1 and S27-1, respectively. The energy levels were determined by using Eq. (6) with the assumption of a constant capture cross section of $\sigma_p = 10^{-16} \text{ cm}^2$. The dashed curves are the extrapolated density distributions without the localized state at about $E_v + 0.3 \text{ eV}$.

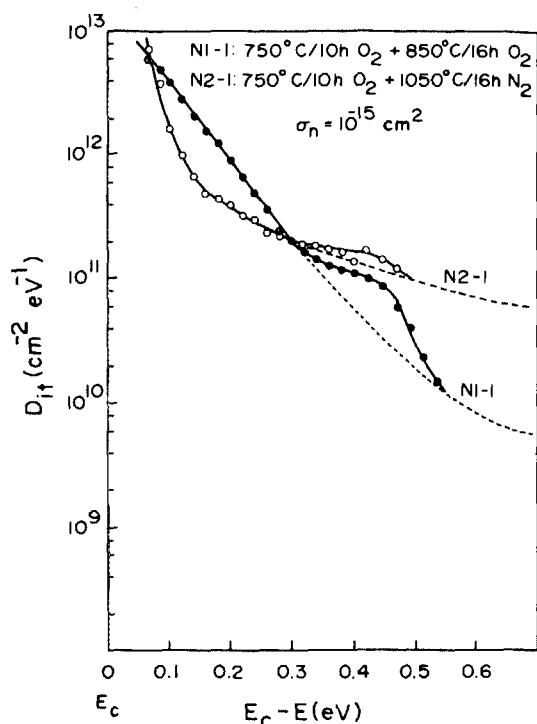


FIG. 8. Density distributions of Si/OP interface states in the upper half of band gap obtained from the DLTS spectra shown in Figs. 4 and 5 for two typical n -type samples, N1-1 and N2-1, respectively. The energy levels were determined by using Eq. (5) with the assumption of a constant capture cross section of $\sigma_n = 10^{-15} \text{ cm}^2$.

lower and the upper half of the band gap, we see that the interface state density has a U-shape distribution similar to that of Si/SiO₂ interface states in MOS structures, in which the density increases toward both band edges with its minimum near midgap. The interface state density near both band edges is of the order of $10^{12} \text{ cm}^{-2} \text{ eV}^{-1}$ which is of the same order of magnitude as that of dry-oxidized Si/SiO₂ interface states.⁵⁸ The density reduction toward midgap is more drastic in low-temperature annealed samples than in high-temperature annealed ones.

The localized states at about $E_v + 0.3 \text{ eV}$ and $E_c - 0.45 \text{ eV}$ seen in Figs. 7 and 8, respectively, are not clearly understood yet. One possible source is a trivalent silicon dangling bond present at the Si/OP interface and the other is a dislocation loop generated around OP's. Both defects form two energy states at similar locations in the band gap.

The localized state at $E_v + 0.3 \text{ eV}$ is often observed in as-oxidized MOS devices and is known to be a trivalent silicon dangling bond state, the so-called P_b center.^{44,49} It has been recently reported^{50,51} that the P_b center has an amphoteric nature, with a donor state at $E_v + 0.3 \text{ eV}$ and an acceptor state at $E_c - 0.25 \text{ eV}$. Thus, the localized state at $E_c - 0.45 \text{ eV}$ may correspond to the acceptor state of P_b center. The energy difference may be attributed to the assumed value of electron capture cross section chosen to determine the energy levels in Fig. 8.

On the other hand, Chan *et al.*²⁸ have recently reported a defect state at $E_c - 0.42 \text{ eV}$ associated with oxygen precipitation in silicon which they suggested to be the dislocation

state. As far as the dislocation-related states are concerned, it is known that dislocations in silicon exhibit two bands of energy states around $E_v + 0.35 \text{ eV}$ and $E_c - 0.38 \text{ eV}$.^{52,53} These energy positions are also very similar to those of the localized states seen in Figs. 7 and 8. There is no clear knowledge about whether the dislocation states are associated with dangling bonds, kinks, or some other electronic structures resulting from reconstruction of dangling bonds along the dislocation core.⁵⁴ But if the dangling bonds cause the electrically active states one might expect that dislocations have the same energy positions as those of the P_b center and the only difference is that one-dimensional periodic dangling bonds along the dislocation core cause two bands of states, while isolated dangling bonds at the Si/OP interfaces cause two discrete energy levels. So, it is difficult to discriminate one from the other in actual measurements.

However, considering the TEM result that dislocation loops are seldom observed in our samples, the localized states are more likely to be related to trivalent dangling bonds than to dislocation loops.

In the low temperature annealed p -type samples, for instance, S7-1,2,3 (800 °C) and S6-1 (950 °C) the density peak near the valence-band edge $E_v + 0.08 \text{ eV}$ is consistently observed on the DLTS spectra as shown in Figs. 1 and 2 as well as on the density plot in Fig. 7. This contrasts with the present knowledge that such a density peak near the band edges does not exist in Si/SiO₂ interface states.^{55,56}

In the midgap energy region the interface state density D_{it} appears to increase with increasing anneal temperature. This is contrary to the temperature dependence of D_{it} for Si/SiO₂ interface states, where D_{it} decreases with increasing oxidation or anneal temperature.^{56,57}

The values of majority-carrier capture cross section used here for the determination of energy levels, 10^{-15} cm^2 for electrons and 10^{-16} cm^2 for holes, were chosen on the basis of previous results measured by the conductance method for wet-oxidized MOS capacitors.⁵⁸ In fact, the capture cross-section values reported for Si/SiO₂ interface states vary depending on sample preparation condition—dry or wet oxidation, post oxidation, or post metallization anneal, etc.—and substrate orientation.^{55,59}

Despite the variation between published values, there seems to be a consensus about the energy dependence of capture cross sections. In the upper half of the band gap, the electron capture cross-section holds constant near midgap and reduces rapidly towards the conduction-band edge.^{55,59,60} The hole capture cross section in the lower half of the band gap increases toward the valence-band edge.^{48,59}

To see the effect of capture cross section on interface state density distributions we show in Figs. 9 and 10 the curves for three different values of capture cross section, 10^{-14} , 10^{-16} , and 10^{-18} cm^2 in the lower and the upper half band gap, respectively. It is seen that the curves shift toward the band edges as the capture cross section decreases and furthermore the shift of the curve is more pronounced near midgap than near the band edges.

It should be pointed out here that in MOS structures there is a unique way to determine the energy levels of Si/SiO₂ interface states independently of the emission process.

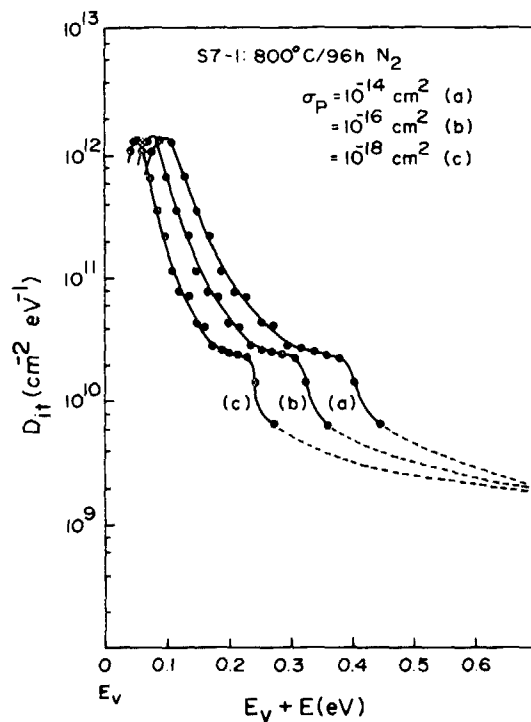


FIG. 9. Effect of the density curve shift in energy for three different hole capture cross sections, $\sigma_P = 10^{-14}$, 10^{-16} , and 10^{-18} cm^2 .

Since the Fermi level at the surface can be adjusted by an externally applied gate voltage, the energy position for a given gate voltage can be determined by computing the corresponding surface potential from the high-frequency $C-V$ data.^{45,48,61} This is not possible in our case, because the surface potential of the silicon adjacent to the OP's cannot be

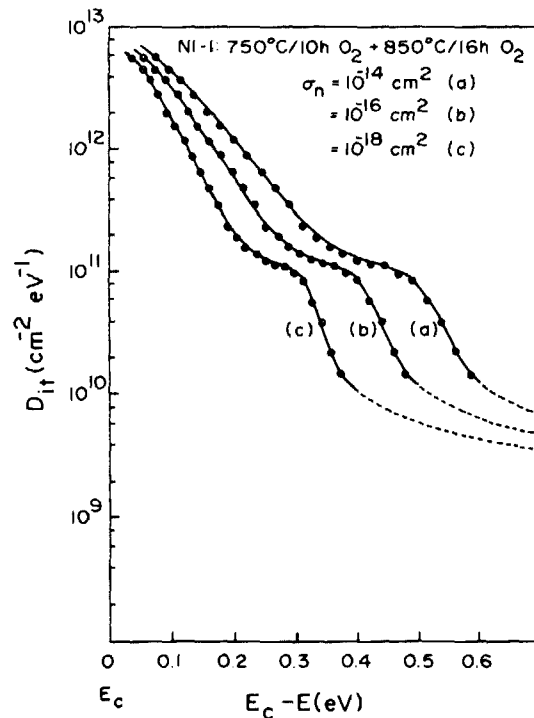


FIG. 10 Effect of the density curve shift in energy for three different electron capture cross sections, $\sigma_n = 10^{-14}$, 10^{-16} , and 10^{-18} cm^2 .

externally controlled. Hence, there is some uncertainty in the energy scale of Figs. 7 and 8.

B. Recombination at oxygen precipitates

Excess minority carriers recombine at oxygen precipitates through interface states, at other bulk impurities such as point defects as well as at the wafer surface via surface states. Hence, the effective recombination lifetime is given by

$$1/\tau_{\text{eff}} = 1/\tau_{\text{op}} + 1/\tau_b + 1/\tau_s, \quad (7)$$

where lifetimes τ_{op} , τ_b , and τ_s characterize the three recombination mechanisms. For surface photovoltage measurements, the surface lifetime is eliminated³⁴ and we have

$$\tau_{\text{eff}} = \tau_{\text{op}} \tau_b / (\tau_{\text{op}} + \tau_b). \quad (8)$$

Our measurements indicate τ_{op} to be the dominant component and τ_{eff} essentially equals τ_{op} .

To evaluate τ_{op} , let us consider the case in which excess carrier recombination takes place only at OP's. Excess carriers generated in the sample diffuse toward OP's and recombine through interface states at the Si/OP interface. We see that this is very much analogous to the precipitation of supersaturated impurity atoms in a solid solution with analogies of excess minority carriers to supersaturated solute atoms, recombination rate to precipitation rate, and lifetime to precipitation time constant. Extensive theoretical work was done on this topic of precipitation by Ham.⁶² Opdorp *et al.* have extended the idea to explain recombination at large defects such as dislocations and metallic precipitates in semiconductors.⁶³ Here we briefly introduce the basic idea.

As schematically shown in Fig. 11, we will consider the ideal case of a periodic array of spherical OP's with radius r_0 that is much smaller than the nearest-neighbor distance. The system is divided into identical simple cubic cells centered on each OP and thus the problem reduces to that of solving the continuity equation for the excess carrier concentration Δn for one cell. The problem can be further simplified by replacing the cubic cell by a spherical cell of radius r_s with equivalent volume, allowing spherically symmetric solutions. Assuming no recombination in the bulk except for that at the Si/OP interface in a specific cell, the continuity equation reduces to the simple diffusion equation

$$\frac{\partial(\Delta n)}{\partial t} = D \nabla^2(\Delta n). \quad (9)$$

This partial differential equation can be solved with one initial condition and two boundary conditions. One boundary condition is obtained on the OP surface in terms of the surface recombination velocity s ,

$$D \nabla(\Delta n) = s(\Delta n) \quad \text{at } r = r_0. \quad (10)$$

The other is obtained on the boundary between neighboring cells where the normal component of current must vanish as a consequence of identical cells,

$$\nabla(\Delta n) = 0 \quad \text{at } r = r_s. \quad (11)$$

By the separation of variables the diffusion Eq. (9) is transformed to an eigenvalue equation for the spatial function $\psi_n(r)$ which satisfies the same boundary conditions,

$$\nabla^2 \psi_n(r) + \lambda_n^2 \psi_n(r) = 0. \quad (12)$$

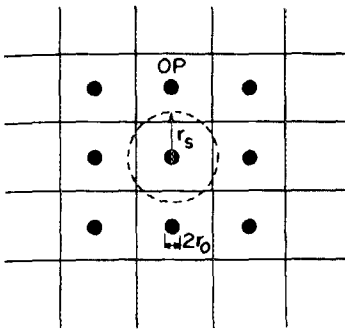


FIG. 11. Schematic illustration of a simple cubic periodic array of spherical OP's. To simplify the problem the cubic cell is approximated to a spherical cell with radius r_s of equivalent volume.

The time-dependent function is given by

$$T(t) = e^{-t/\tau_n}, \quad (13)$$

where τ_n is related to λ_n by

$$\lambda_n^2 = 1/\tau_n D. \quad (14)$$

The solutions of Eq. (12) take a spherically symmetric form such as

$$\psi_n(r) = A_n [\sin \lambda_n (r - B_n)/r], \quad (15)$$

where A_n denotes a normalization constant and B_n a constant that can be determined from the boundary conditions. The validity of Eq. (15) as a solution can be immediately checked by substituting Eq. (15) into Eq. (12) with the proper Laplacian for the spherically symmetric case. The eigenvalues λ_n can also be determined from the boundary conditions. The general solution for $\Delta n(r, t)$ is given by the superposition of eigenfunctions:

$$\Delta n(r, t) = \sum_{n=0}^{\infty} a_n \psi_n(r) e^{-t/\tau_n}, \quad (16)$$

where a_n are the expansion coefficients that may be determined from the initial distribution of excess carriers, using the orthogonality property of eigenfunctions.

Since for $r_0/r_s \ll 1$, true for most of the cases, the terms of $n \geq 1$ in Eq. (16) decay very fast; after a short period of time, Eq. (16) will be left with the first term for the fundamental mode $n = 0$ so that the average excess carrier concentration will decay in a simple exponential function with the fundamental time constant τ_0 . Ham⁶² has shown the eigenvalue for $n = 0$ to be

$$\lambda_0 = 3r_0/[r_s^3(1 + D/sr_0)]. \quad (17)$$

Using Eq. (14) and the relation between r_s and OP density, $N_{op} = 1/(\frac{4}{3}\pi r_s^3)$, gives an expression for the time constant τ_0 that is essentially the same as the effective excess carrier lifetime due to recombination at OP's:

$$\tau_{op} = (1/4\pi N_{op} D r_0) + (1/4\pi N_{op} s r_0^2), \quad (18)$$

where the first term is for diffusion and the second term for surface recombination. If $D \gg sr_0$, surface recombination will be the rate-limiting process, whereas for $sr_0 \gg D$, diffusion will be the rate-limiting process. The latter situation arises in many precipitation cases of supersaturated impuri-

ty atoms in a solid solution. However, in the cases of excess carrier recombination in elementary semiconductors such as Ge and Si, with which we are concerned, the former condition is generally satisfied.⁶³ Hence Eq. (18) is approximated by

$$\tau_{op} \approx (4\pi N_{op} s r_0^2)^{-1}. \quad (19)$$

So far we have discussed the transient lifetime of excess carrier decay after an external excitation is turned off. The SPV technique is a steady-state technique. Although OP's may cause some spatial fluctuation of the excess carrier concentration, i.e., minimum at the OP surface and maximum in the midregion between two neighboring OP's, the photovoltage measured in the SPV technique is related to an average excess carrier concentration at the edge of the surface depletion region. The average excess carrier concentration in the bulk, far from the surface where the surface effect on excess carrier distribution may be neglected, is given by the product of a generation rate g and a steady-state effective lifetime τ_{eff} , due to recombination at OP's, i.e., $\bar{\Delta n} = g\tau_{eff}$. Here, we will show that the steady-state effective recombination lifetime is also given by the same formula as Eq. (18). Assuming the excess carrier recombination to take place only at OP's, the steady-state continuity equation in a spherical cell may be written as

$$D\nabla^2(\Delta n) + g = 0. \quad (20)$$

Since the Laplacian for spherically symmetric cases is given by

$$\nabla^2(\Delta n) = \frac{1}{r^2} \frac{\partial}{\partial r} \left(r^2 \frac{\partial \Delta n}{\partial r} \right), \quad (21)$$

the excess carrier distribution in the cell centered by an OP is obtained by integrating Eq. (20) twice with the same boundary conditions as previously given by Eqs. (10) and (11):

$$\begin{aligned} \Delta n(r) = \frac{g}{3D} \left[r_s^3 \left(\frac{1}{r_0} - \frac{1}{r} \right) + \frac{1}{2} (r_0^2 - r^2) \right] \\ + \frac{gr_0}{3s} \left[\left(\frac{r_s}{r_0} \right)^3 - 1 \right]. \end{aligned} \quad (22)$$

Then, the average excess carrier concentration $\bar{\Delta n}$ is

$$\bar{\Delta n} = \frac{1}{V_s} \int_{r_0}^{r_s} 4\pi r^2 n(r) dr, \quad (23)$$

where V_s is the cell volume. For $r_s/r_0 \gg 1$ the result of the above integration can be shown to give

$$\bar{\Delta n} = g \left[(1/4\pi D r_0 N_{op}) + (1/4\pi r_0^2 s N_{op}) \right], \quad (24)$$

where we also used $(N_{op})(\frac{4}{3}\pi r_s^3) = 1$.

It can be seen that the expression in the bracket of Eq. (24) corresponds to an effective steady-state recombination lifetime which is exactly the same as that in Eq. (18). Therefore, in the SPV measurements where the surface effect on excess carrier distribution must be taken into account, the average excess carrier concentration at the surface space-charge region edge to which the surface photovoltage is related, may be obtained by solving the following continuity equation for $\bar{\Delta n}$

$$D \frac{d^2(\Delta n)}{dx^2} - \frac{\Delta n}{\tau_{\text{eff}}} + g = 0. \quad (25)$$

This indicates that a diffusion length measured by the SPV technique is interpreted as $L = \sqrt{D\tau_{\text{eff}}}$.

What causes the different lifetime values between *p*-Si and *n*-Si, even for almost identical size and density of OP's? Considering Eq. (19) for the effective lifetime there are two possible factors that can cause the lifetime difference. One is the capture cross section of Si/OP interface states. In general, it can vary by two or three orders of magnitude due to the different charge states depending on the position of Fermi level.⁶⁴ The other is a band bending around OP's that is caused by positive fixed charges in OP's with SiO_x composition. In MOS structures a fixed charge is known to exist in the oxide layer near the Si/SiO₂ interface and is positively charged.⁶⁵ This fixed oxide charge is also known to originate from silicon dangling bonds on the oxide side due to excess silicon that gives rise to an energy state well above the silicon conduction-band edge.⁶⁶ So, it is positively charged by donating electrons to the silicon conduction band and can hardly be recharged by electrons over a wide range of surface potential.

If the capture cross section is assumed to be the major cause for the lifetime difference, whose effect is included in the surface recombination velocity *s*, the surface recombination velocity in *p*-type samples is calculated to be about 10⁷ cm/s, using Eq. (19) with measured *N*_{op}, *r*₀, and *τ*_{eff}. This value is equal to the average thermal velocity of electrons at room temperature which is the kinetic limit⁶⁷ for the surface recombination velocity, indicating that this assumption is not valid.

Therefore, it is plausible to assume that the band bending around OP's due to the positive fixed charges is the major cause for the lifetime difference. Figure 12 schematically shows the band diagrams around OP's due to positive fixed charges. In *p*-type samples a depletion region is formed around the OP's, providing a large collecting volume for minority electrons while in *n*-type samples an accumulation layer is established near OP's, acting as a reflecting barrier to minority holes.

In order to see how the depletion region volume is quantitatively related to the positive fixed charge density *Q_f* and thus to the band bending in *p*-type silicon we solve Poisson's equation in spherical coordinates. For the spherically symmetric cases, Poisson's equation is given by

$$\frac{1}{r^2} \frac{\partial}{\partial r} \left(r^2 \frac{\partial \phi}{\partial r} \right) = \frac{qN_A}{\epsilon_s}. \quad (26)$$

Double integration of Eq. (26) with the boundary condition that the electric field vanishes at the depletion edge gives the following relationship:

$$\phi_0 = \frac{qN_A r_0^2}{3\epsilon_s} \left[\left(\frac{r_d}{r_0} \right)^3 - \frac{3}{2} \left(\frac{r_d}{r_0} \right)^2 + \frac{1}{2} \right], \quad (27)$$

where ϕ_0 is the band bending measured by the potential difference between the bulk and the interface [see Fig. 12(a)], *r*₀ and *r_d* are the OP and space-charge region radius, respectively.

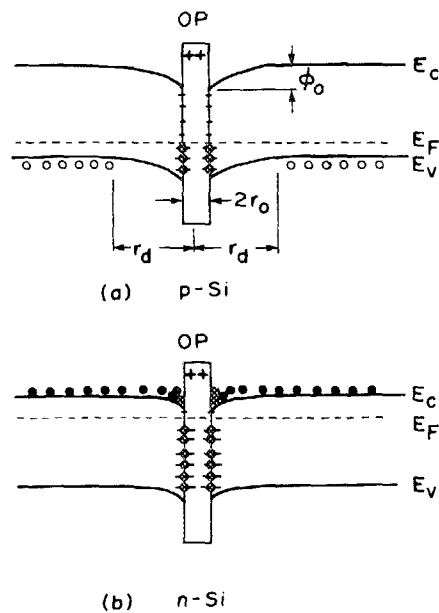


FIG. 12. Schematic band diagrams with band bending due to positive fixed charges in OP's which gives rise to (a) a depletion region in *p*-Si and (b) an accumulation layer around OP's in *n*-Si.

From charge neutrality considerations, where the total positive charges must equal the total negative charges, we obtain the relationship between the fixed charge density per unit area *Q_f* and the space-charge region radius,

$$Q_f = \frac{N_A}{3} r_d \left(\frac{r_d}{r_0} \right)^2 \left[1 - \left(\frac{r_0}{r_d} \right)^3 \right]. \quad (28)$$

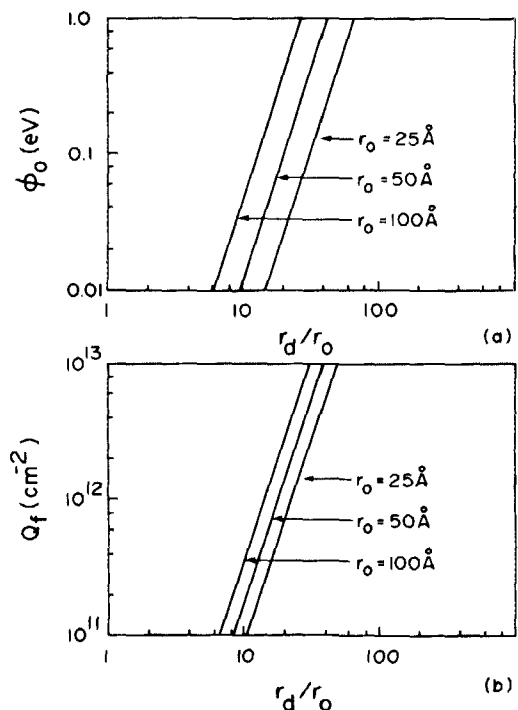


FIG. 13. (a) plot of ϕ_0 vs r_d/r_0 and (b) plot of Q_f vs r_d/r_0 in *p*-Si using Eqs. (27) and (28), respectively, for three different OP sizes, $r_0 = 25, 50,$ and 100 \AA . The doping concentration of $N_A = 10^{15} \text{ cm}^{-3}$ was used.

Equations (27) and (28) are illustrated in Figs. 13(a) and 13(b), respectively, for three specific OP radii, $r_0 = 25, 50$, and 100 \AA , where $N_A = 10^{15} \text{ cm}^{-3}$ was used. When there exists a depletion region around OP's, then, the boundary condition given by Eq. (10) is not valid any more because an electric field is present at the Si/OP interface. A new boundary condition at the depletion region edge must be used to solve the diffusion equation given by Eq. (9)⁶⁸:

$$D\nabla(\Delta n) = s_{\text{eff}}(\Delta n) \quad \text{at} \quad r = r_d. \quad (29)$$

The resulting expression for τ_{op} is obtained by replacing r_0 by r_d and s the surface recombination velocity at the Si/OP interface by s_{eff} an effective recombination velocity at the depletion boundary, i.e.,

$$\tau_{\text{op}} = 1/4\pi r_d^2 s_{\text{eff}} N_{\text{op}}. \quad (30)$$

In p -type silicon, the effective surface recombination velocities are calculated using Eq. (30) with the measured values of N_{op} and τ_{eff} , and the estimated value of r_d for $Q_f = 10^{12} \text{ cm}^{-2}$ which is a typical value in as-oxidized Si/SiO₂ structures.⁵⁶ In Table V are summarized the calculated values for a few samples with data available. They are of the orders of 10^4 – 10^5 cm/s . It is noteworthy that the values are of the same order of magnitudes as those at the depletion edge of grain boundaries in polysilicon⁶⁷ measured by the EBIC technique and those at the surface of MOS structures obtained from peak forward current in gated diodes.⁶⁹

In n -type samples, the situation becomes more complicated in the sense of applying the model to this accumulation case. One difficulty is in determining the space-charge region radius that may be a few extrinsic Debye lengths as expected from the one-dimensional problem. However, taking into consideration the acceptorlike behavior of interface states in the upper half of the band gap⁵⁶ such that some of the positive fixed charges may be compensated by the negatively charged interface states, we expect that the band bending may be less significant compared to p -type cases. For simplicity, we assume the flat-band condition to calculate the surface recombination velocities for n -type samples. The calculated values for two samples, N2-1 and N2-2, are also shown in Table V. But it should be kept in mind that a band bending, although small for the above reason, acts as a reflecting barrier to minority holes so that the actual surface recombination velocities must be smaller than the calculated ones.

V. SUMMARY

IR absorption, TEM, DLTS, and SPV techniques have been used to study recombination properties in oxygen-pre-

cipitated silicon. We have observed that once interstitial oxygen precipitates in the silicon bulk, the minority-carrier recombination lifetime reduces drastically and the degree of lifetime degradation is much more pronounced in p -Si than in n -Si.

DLTS results show a continuous distribution of energy states in the band gap. TEM results show the oxygen precipitates to be the dominant structural defects while dislocation loops and stacking faults are seldom observed in the samples under consideration. Therefore, we conclude that the continuous DLTS spectra are due to Si/OP interface states which are the major recombination centers responsible for lifetime degradation.

We have obtained the density distributions $D_{it}(E)$ of Si/OP interface states from the DLTS spectra under the assumption of constant values for the capture cross section. The Si/OP interface states are found to be similar to the as-oxidized Si/SiO₂ interface states in some respects, such as the U-shaped distribution of D_{it} and the localized states due to the trivalent-silicon dangling bond, known as the P_b center. On the other hand, we also find some inconsistent properties between the interface states of these two structures. The density peak at $E_v + 0.08 \text{ eV}$ in the samples annealed at low temperatures like 800 or 950 °C is known not to exist at the Si/SiO₂ interface. As another example, D_{it} near the mid-gap of the Si/OP interface states increase with anneal temperature while that for Si/SiO₂ interface states is known to decrease with oxidation or anneal temperature.

A model for recombination at OP's has been presented in terms of the surface recombination velocity at Si/OP interfaces and their average density and size. To explain the lifetime difference between p -Si and n -Si we have postulated the existence of positive fixed charges in OP's similar to the oxide charges in the oxide near the Si/SiO₂ interface. These positive fixed charges give rise to a depletion region around OP's in p -Si, providing a large collecting volume for minority electrons, but an accumulation layer in n -Si, acting as a reflecting barrier to minority holes.

Assuming $Q_f = 10^{12} \text{ cm}^{-2}$ as a typical value of positive fixed charge density on the oxygen precipitate surfaces, the model explains the nanosecond order of recombination lifetimes measured for p -type silicon with 10^4 – 10^5 cm/s of the effective recombination velocity at the depletion boundary around OP's reasonably well. These recombination velocity values are of the same order of magnitude as those measured at the grain boundaries in polysilicon and at the as-oxidized Si/SiO₂ interfaces.

ACKNOWLEDGMENTS

We would like to thank A. M. Goodman from RCA Labs for the SPV measurements, C. J. Varker from Motorola SRDL for Si wafers and fruitful discussions, H. L. Tsai from Texas Instruments Central Research Laboratories for the TEM measurements, J. B. Marion and J. S. Kang from ASU Center for Solid-State Electronics for experimental expertise, and L. Arneson for typing this paper.

¹S. M. Hu, J. Vac. Sci. Technol. **14**, 17 (1977).

²J. W. Corbett, R. S. McDonald, and G. D. Watkins, J. Phys. Chem. Solids **25**, 873 (1964).

TABLE V. Calculated s_{eff} using Eqs. (19) and (30).

Sample	N_{op} (cm^{-3})	r_0 (\AA)	τ_{eff} (ns)	s_{eff} (cm/s)	ϕ_0 (V)
S7-1 (p)	3.0×10^{13}	54	0.65	4.3×10^4	0.07
S7-2 (p)	2.6×10^{13}	54	0.85	3.8×10^4	0.07
S27-1 (p)	2.6×10^{12}	100	1.92	5.0×10^4	0.14
S27-2 (p)	1.7×10^{12}	120	1.76	1.1×10^5	0.14
N2-1 (n)	1.1×10^{12}	125	510	9.0×10^4	
N2-2 (n)	2.3×10^{12}	100	790	4.4×10^4	

- ³P. E. Freeland, K. A. Jackson, C. W. Lowe, and J. R. Patel, *Appl. Phys. Lett.* **30**, 31 (1977).
- ⁴J. Osaka, N. Inoue, and K. Wada, *Appl. Phys. Lett.* **36**, 288 (1980).
- ⁵Y. Matsushita, *J. Cryst. Growth* **56**, 516 (1982).
- ⁶K. Wada and N. Inoue, *J. Cryst. Growth* **49**, 749 (1980).
- ⁷S. Kishino, Y. Matsushita, M. Kanamori, and T. Iizuka, *Jpn. J. Appl. Phys.* **21**, 1 (1982).
- ⁸J. R. Patel, *Semiconductor Silicon 1981*, edited by H. R. Huff, R. J. Kriegler, and Y. Takeishi (Electrochemical Society, Princeton, NJ, 1981), p. 189.
- ⁹T. Y. Tan and W. K. Tiel, *Philos. Mag.* **34**, 615 (1976).
- ¹⁰D. M. Maher, A. Staudinger, and J. R. Patel, *J. Appl. Phys.* **47**, 3813 (1976).
- ¹¹F. Shimura, *J. Cryst. Growth* **54**, 588 (1981).
- ¹²H. L. Tsai and R. W. Carpenter, *Proceedings of the 41st Annual Meeting of the Electron Microscopy Society of America*, edited by G. W. Bailey (San Francisco Press, San Francisco, CA, 1983), p. 152.
- ¹³F. A. Ponce, T. Yamashita, and S. Hahn, *Appl. Phys. Lett.* **43**, 1051 (1983).
- ¹⁴P. Gaworjewski, E. Hild, F. G. Kirscht, and L. Vecsernyes, *Phys. Status Solidi A* **85**, 133 (1984).
- ¹⁵K. Tempelhoff, F. Spiegelberg, R. Gleichmann, and D. Wruck, *Phys. Status Solidi A* **56**, 213 (1979).
- ¹⁶A. Bourret, J. Thibault-Desseaux, and D. N. Seidman, *J. Appl. Phys.* **55**, 825 (1984).
- ¹⁷S. M. Hu, *J. Appl. Phys.* **51**, 5945 (1981).
- ¹⁸S. Mahajan, G. A. Rozgonyi, and D. Brosen, *Appl. Phys. Lett.* **30**, 73 (1977).
- ¹⁹J. R. Patel, K. A. Jackson, and H. Reiss, *J. Appl. Phys.* **48**, 5279 (1977).
- ²⁰K. Wada, H. Takaoka, N. Inoue, and K. Kohra, *Jpn. J. Appl. Phys.* **18**, 1629 (1979).
- ²¹J. H. Matlock, *Defects in Silicon*, edited by W. M. Bullis and L. C. Kimerling (Electrochemical Society, Pennington, NJ, 1983), p. 3.
- ²²K. H. Yang, H. F. Kappert, and G. H. Schwuttke, *Phys. Status Solidi A* **50**, 221 (1978).
- ²³D. K. Schroder, J. D. Whitfield, and C. J. Varker, *IEEE Trans. Electron Devices* **ED-31**, 463 (1984).
- ²⁴C. J. Varker, J. D. Whitfield, and P. Fejes, *Material Research Society Symposium Proceedings*, Vol. 14, edited by S. Mahajan and J. W. Corbett (North-Holland, NY, 1983), p. 187.
- ²⁵M. Miyagi, K. Wada, J. Osaka, and N. Inoue, *Appl. Phys. Lett.* **40**, 719 (1982).
- ²⁶D. K. Schroder, J. M. Hwang, J. S. Kang, A. M. Goodman, and B. L. Sopori, *VLSI Science and Technology 85*, edited by W. M. Bullis and S. Broydo (Electrochemical Society, Princeton, NJ, 1985), p. 419.
- ²⁷S. N. Chakravarti, P. L. Garbarino, and K. Murty, *Appl. Phys. Lett.* **40**, 581 (1982).
- ²⁸S. S. Chan, C. J. Varker, J. D. Whitfield, and R. W. Carpenter, *Materials Research Society Symposium Proceedings*, Vol. 46, edited by N. M. Johnson, S. G. Bishop, and G. D. Watkins (North-Holland, NY, 1985), p. 281.
- ²⁹K. Hoelzlein, G. Pensl, and M. Schulz, *Appl. Phys. A* **34**, 155 (1984).
- ³⁰S. M. Hu, *J. Appl. Phys.* **51**, 3666 (1980).
- ³¹F. Shimura, *Appl. Phys. Lett.* **39**, 987 (1981).
- ³²G. L. Miller, D. V. Lang, and L. C. Kimerling, *Ann. Rev. Mater. Sci.* **7**, 377 (1977).
- ³³A. Rohatgi, J. R. Davis, R. H. Hopkins, and P. G. McMullin, *Solid-State Electron.* **26**, 1039 (1983).
- ³⁴A. M. Goodman, L. A. Goodman, and H. F. Gossenberger, *RCA Rev.* **44**, 326 (1983).
- ³⁵R. A. Craven, *Semiconductor Silicon 1981*, edited by H. R. Huff, R. J. Kriegler, and Y. Takeishi (Electrochemical Society, Princeton, NJ, 1981), p. 254.
- ³⁶R. C. Newman, M. J. Binns, W. P. Brown, F. M. Livingston, S. Messoras, R. J. Stewart, and J. G. Wilkes, *Physica* **116B**, 264 (1983).
- ³⁷T. Y. Tan, E. E. Gardner, and W. K. Tice, *Appl. Phys. Lett.* **30**, 175 (1977).
- ³⁸J. Andrews, *Defects in Silicon*, edited by W. M. Bullis and L. C. Kimerling (Electrochemical Society, Pennington, NJ, 1983), p. 133.
- ³⁹D. K. Schroder, *Solid-State Electron.* **27**, 247 (1984).
- ⁴⁰U. Goesele and T. Y. Tan, *Appl. Phys. A* **28**, 79 (1982).
- ⁴¹R. C. Newman, A. S. Oates, and F. M. Livingston, *J. Phys. C* **16**, L667 (1983).
- ⁴²K. L. Brower, *Phys. Rev. B* **14**, 872 (1976).
- ⁴³L. C. Kimerling, *Inst. Phys. Conf. Ser.* **31**, 221 (1977).
- ⁴⁴N. M. Johnson, D. J. Bartelink, and M. Schulz, *The Physics of SiO₂ and Its Interfaces*, edited by S. T. Pantelides (Pergamon, New York, 1978), p. 421.
- ⁴⁵N. M. Johnson, *Appl. Phys. Lett.* **34**, 802 (1979).
- ⁴⁶T. J. Tredwell and C. R. Viswanathan, *Appl. Phys. Lett.* **36**, 426 (1980).
- ⁴⁷K. L. Wang, *IEEE Trans. Electron Devices* **ED-27**, 2231 (1980).
- ⁴⁸W. D. Eades and R. M. Swanson, *J. Appl. Phys.* **56**, 1744 (1984).
- ⁴⁹N. M. Johnson, D. J. Bartelink, and J. P. McVittie, *J. Vac. Sci. Technol.* **16**, 1407 (1979).
- ⁵⁰N. M. Johnson, D. K. Biegelsen, M. D. Moyer, S. T. Chang, E. H. Poindexter, and P. J. Caplan, *Appl. Phys. Lett.* **43**, 563 (1983).
- ⁵¹E. H. Poindexter, G. J. Gerardi, M. E. Rueckel, P. J. Caplan, N. M. Johnson, and D. K. Biegelsen, *J. Appl. Phys.* **56**, 2844 (1984).
- ⁵²L. C. Kimerling and J. R. Patel, *Appl. Phys. Lett.* **34**, 73 (1979).
- ⁵³V. A. Grazhulis, V. V. Kueder, and V. Yu. Mukhina, *Phys. Status Solidi A* **43**, 407 (1977).
- ⁵⁴A. Ourmazd, *Contemp. Phys.* **25**, 251 (1984).
- ⁵⁵H. Deuling, E. Kausmann, and A. Goetzberger, *Solid-State Electron.* **15**, 559 (1972).
- ⁵⁶Y. C. Cheng, *Prog. Surf. Sci.* **8**, 181 (1977).
- ⁵⁷R. R. Razouk and B. E. Deal, *J. Electrochem. Soc.* **126**, 1573 (1979).
- ⁵⁸E. H. Nicollian and A. Goetzberger, *Bell Syst. Tech. J.* **46**, 1055 (1967).
- ⁵⁹M. Schulz, *Surf. Sci.* **132**, 422 (1983).
- ⁶⁰R. J. Kriegler, T. F. Devenyi, K. D. Chik, and J. Shappir, *J. Appl. Phys.* **50**, 398 (1979).
- ⁶¹A. Goetzberger, E. Klausmann, and M. Schulz, *CRC Crit. Rev.* **6**, 1 (Jan. 1976).
- ⁶²F. S. Ham, *J. Phys. Chem. Solids* **6**, 335 (1958).
- ⁶³A. T. Vink, C. J. Werkhaven, and C. V. Opdorp, *Semiconductor Characterization Techniques*, edited by P. A. Barnes and G. A. Rozgonyi (Electrochemical Society Softbound Proceedings Series, Princeton, NJ, 1978), p. 259.
- ⁶⁴A. G. Milnes, *Deep Impurities in Semiconductors* (Wiley, New York, 1973), Chap. 5.
- ⁶⁵B. E. Deal, *J. Electrochem. Soc.* **121**, 198 C (1974).
- ⁶⁶C. M. Svenson, *The Physics of SiO₂ and Its Interface*, edited by S. T. Pantelides (Pergamon, New York, 1978), p. 328.
- ⁶⁷D. E. Burk, S. Kanner, J. E. Muyschoudt, D. S. Shaulis, and P. E. Russell, *J. Appl. Phys.* **54**, 169 (1983).
- ⁶⁸D. J. Fitzgerald and A. S. Grove, *Surf. Sci.* **9**, 347 (1968).
- ⁶⁹L. L. Rosier, *IEEE Trans. Electron Devices* **ED-13**, 260 (1966).